ADVANCED FUNCTIONAL MATERIALS
www.afm-journal.de



# 3D Shape-Morphing Display Enabled by Electrothermally Responsive, Stiffness-Tunable Liquid Metal Platform with Stretchable Electroluminescent Device

*Subin Oh, Sunwoo Lee, Sang-Hyuk Byun, Simok Lee, Choong Yeon Kim, Junwoo Yea, Sein Chung, Shuo Li, Kyung-In Jang, Jiheong Kang,* and Jae-Woong Jeong**

**3D displays are of great interest as next-generation displays by providing intensified realism of 3D visual information and haptic perception. However, challenges lie in implementing 3D displays due to the limitation of conventional display manufacturing technologies that restrict the dimensional scaling of their forms beyond the 2D layout. Furthermore, on account of the inherent static mechanical properties of constituent materials, the current display form factors can hardly achieve robust and complex 3D structures, thereby hindering their diversity in morphologies and applications. Herein, a versatile shape-morphing display is presented that can reconfigure its shape into various complex 3D structures through electrothermal operation and firmly maintain its morphed states without power consumption. To achieve this, a shape-morphing platform, which is composed of a low melting point alloy (LMPA)-graphene nanoplatelets (GNPs)-elastomer composite, is integrated with a stretchable electroluminescent (EL) device. The LMPA in the composite, the key material for variable stiffness, imparts shape memory property and forms conductive pathways with GNPs enabling rapid electrothermal actuation. The stretchable EL device provides reliable illumination in 3D shape implementations. Experimental studies and proof-of-concept demonstrations show the potential of the shape-morphing display, opening new opportunities for 3D art displays, transformative wearable electronics, and visio-tactile automotive interfaces.**

## 1. Introduction

The display plays an important role as a human-machine interface in various fields such as for mobile devices, wearable electronics, media art, automotive interfaces, and many others.[1–3] Recent advancements in display technology have aimed to enhance user experience and convenience. For example, displays have evolved from the rigid flat form to bendable, rollable, foldable, and stretchable forms for increased portability and accessibility.[4] Furthermore, new wearable display platforms, involving textile-based displays[5–7] and skin-inspired electronics,[8,9] have been developed to offer opportunities for greater user intimacy to enable ubiquitous physiological monitoring and healthcare. However, the two-dimensional (2D) planar nature of these technologies has limitations in terms of depth perception and realism.

For enhanced user experience in real-world applications, three-dimensional (3D) displays have attracted a great deal of attention as the next-generation displays that can bring out a more engaging and interactive experience by allowing for displaying 3D images on a non-flat surface. The current display manufacturing technologies, which are largely dependent on the traditional 2D fabrication processes, however, restrain the design of arbitrary shapes of 3D displays. Recent research in materials and micro/nano fabrication has tried to overcome this fundamental limitation by developing strategies for reconfiguring 2D planar electronics into 3D shapes. For example, researchers investigated various approaches for the 2D-to-3D reconfiguration based on thermoforming,[10–12] kirigami,[13–15] origami,[16–20] buckling,[21,22] 4D printing,[23,24] and stimuli-responsive materials.[25–28] Despite these transformation methods, 3D displays that adopt the

S. Oh, S.-H. Byun, S. Lee, C. Y. Kim, J.-W. Jeong
School of Electrical Engineering
Korea Advanced Institute of Science and Technology
Daejeon 34141, Republic of Korea
E-mail: jjeong1@kaist.ac.kr

S. Lee, J. Kang
Department of Materials Science and Engineering
Korea Advanced Institute of Science and Technology
Daejeon 34141, Republic of Korea
E-mail: jiheongkang@kaist.ac.kr

The ORCID identification number(s) for the author(s) of this article can be found under https://doi.org/10.1002/adfm.202214766.

J. Yea, K.-I. Jang
Department of Robotics Engineering
Daegu Gyeongbuk Institute of Science and Technology
Daegu 42988, Republic of Korea

S. Chung
Department of Chemical Engineering
Pohang University of Science and Technology
Pohang 37673, Republic of Korea

S. Li
Querrey Simpson Institute for Bioelectronics
Northwestern University
Evanston, IL 60208, USA

DOI: 10.1002/adfm.202214766

 

existing electronic form factors—that is, either rigid, bendable, or stretchable forms—are challenging to provide robust yet reconfigurable 3D interfaces with high structural sophistication. The biggest challenge is from their inherent static mechanical properties that can scarcely achieve 3D configurations with both high structural complexity and free-standing mechanical stability with high load-bearability. For example, both rigid and bendable 3D displays provide the convenience of device operation and mechanical robustness to maintain their shapes, but in exchange, they are nearly impossible to transform their shape into complicated 3D mesostructures. On the other hand, the opposite aspect is shown in stretchable 3D displays. Stretchable displays can conformally and seamlessly integrate on various curvilinear 3D surfaces to implement complex 3D displays due to their high deformability and conformity.[29,30] However, such displays are inappropriate for off-body or off-object applications because of their innate mechanical compliance and elasticity, making them unable to retain their morphed states in a free-standing condition.

One of the most prospective approaches to implementing versatile, robust 3D displays may be utilizing platforms that can tune their shape and rigidity in order to make them encompass the advantageous features of both rigid and soft electronics[31–33] to maximize their utility. Here, we report a new class of shape-morphing displays (SMDs) that can bring users realistic visual information as well as enhanced physical interaction from tangible 3D configurations. The SMD in a 2D form can be transformed into complex 3D structures through electrothermal activation and firmly maintain its deformed shapes while reversibly achieving reconfigurations. This ability enables not only the facile realization of desired 3D-shaped display for specific applications but also the on-demand conversion of display function (i.e., switching between wearable and handheld display), making it highly adaptable and versatile. Our SMD combines a stretchable alternating current electroluminescent (ACEL) device with an electrothermal shape-morphing platform (eSMP) that can create various 3D configurations. The eSMP, which uses an elastomer composite that embeds low melting point alloy (LMPA) and Graphene nanoplatelets (GNPs), allows for variable stiffness and shape memory while also providing enhanced electrical and thermal conductivity for energy-efficient operation. We chose Field's metal (FM) as the LMPA for its optimal melting point (62°C) and ability to maintain a reliable solid state at room temperature.[48] Taking advantage of versatile shape reconfigurability along with stable light emission, we have successfully demonstrated a series of SMDs for transformative wearable displays, 3D art displays, and touch-sensing automotive 3D displays to show the potential of SMDs. We envision that SMDs will bring out unprecedented form factors for the next-generation displays and pave a new way for a wide variety of applications.

## 2. Results and Discussions

### 2.1. Concept and Design of SMD

**Figure 1**a illustrates the concept and operational principle of the SMD, which features rapid multi-morphological reconfigurability and shape fixation based on thermal field-induced stiffness modulation. The shape programming is realized through the two-step operation mechanism: that is, shape-morphing and shape-holding. In the "shape-morphing" step, the 2D planar SMD is heated to a temperature above the FM melting point for softening which allows it to morph into any complex 3D structure. Then, the subsequent cooling of the deformed SMD enables the "shape-holding", giving rise to its soft-to-rigid conversion. As a result, the morphed 3D structure can firmly maintain its shape and be used for the desired purpose requiring a specific configuration with mechanical robustness. The morphed SMD can recover to its original flat state or convert to different structural shapes repeatedly by heating. Through this reversible programmable mechanism, our SMD can provide complicated 3D morphologies and achieve customizable shape modulation. Following our operational approach, the SMD can potentially be applied in a variety of fields—including a transformative wearable display, shape morphable 3D art display, and a visio-tactile automotive interface—to open new opportunities for versatile displays as well as facile fabrication of unusual 3D displays starting from the traditional 2D layouts. Some potential applications of the SMD technology include a transformative display that can covert between the wearable and the handheld mode, a shape morphable 3D art display that enables programmable actuation such as a flower blooming, and a visio-tactile automotive interface providing the multisensory perception of information.

The SMD consists of two main functional parts: i) an eSMP for reversible shape reconfiguration and fixation and ii) a stretchable ACEL device for light-emitting (Figure 1b). A cross-sectional optical microscopy image shows the resulting structure of the SMD (Figure S1a, Supporting Information). The eSMP is a core shape reconfigurable component that enables its unique stiffness tunability and shape memory mechanism. To develop the shape-morphable system, mechanically tunable materials, including liquid crystal elastomers,[34] shape memory polymers,[35] magnetorheological fluid (MRF),[36] and jamming materials,[37] have been actively studied. Among those, composite materials based on liquid metals[38–42,45] have shown promise as a key enabler for variable stiffness based on their wide range of elastic modulus regulation (1 to $10^{10}$ Pa) and power-efficient, reversible solid-liquid phase transition. For this reason, we established an elastomeric composite including liquid metal (more specifically, LMPA) microparticles in polydimethylsiloxane (PDMS; Sylgard 184, Dow Corning) to create the eSMP (Figure S1b, Supporting Information). Field's metal, which is fusible eutectic bismuth (Bi)-based alloy of Bi (32.5 wt.%), indium (In) (51 wt.%), and tin (Sn) (16.5 wt.%), is chosen as the LMPA due to its high elastic modulus (≈9.25 GPa) in the solid state and negligible modulus in the liquid state,[48] low toxicity,[49] and relatively low melting point (≈62 °C),[48] which allows robust yet energy-efficient phase change independent of the ambient temperature of various environments (i.e., negative to ≈50 °C). Accordingly, the FM microparticles-embedded platform can easily change its shape, flexibility, and stretchability at nearly or above 62 °C through the dynamic solid-to-liquid phase transition and hold the new configuration via rapid solidification of the FM below its melting temperature. In order to enhance both the electrical

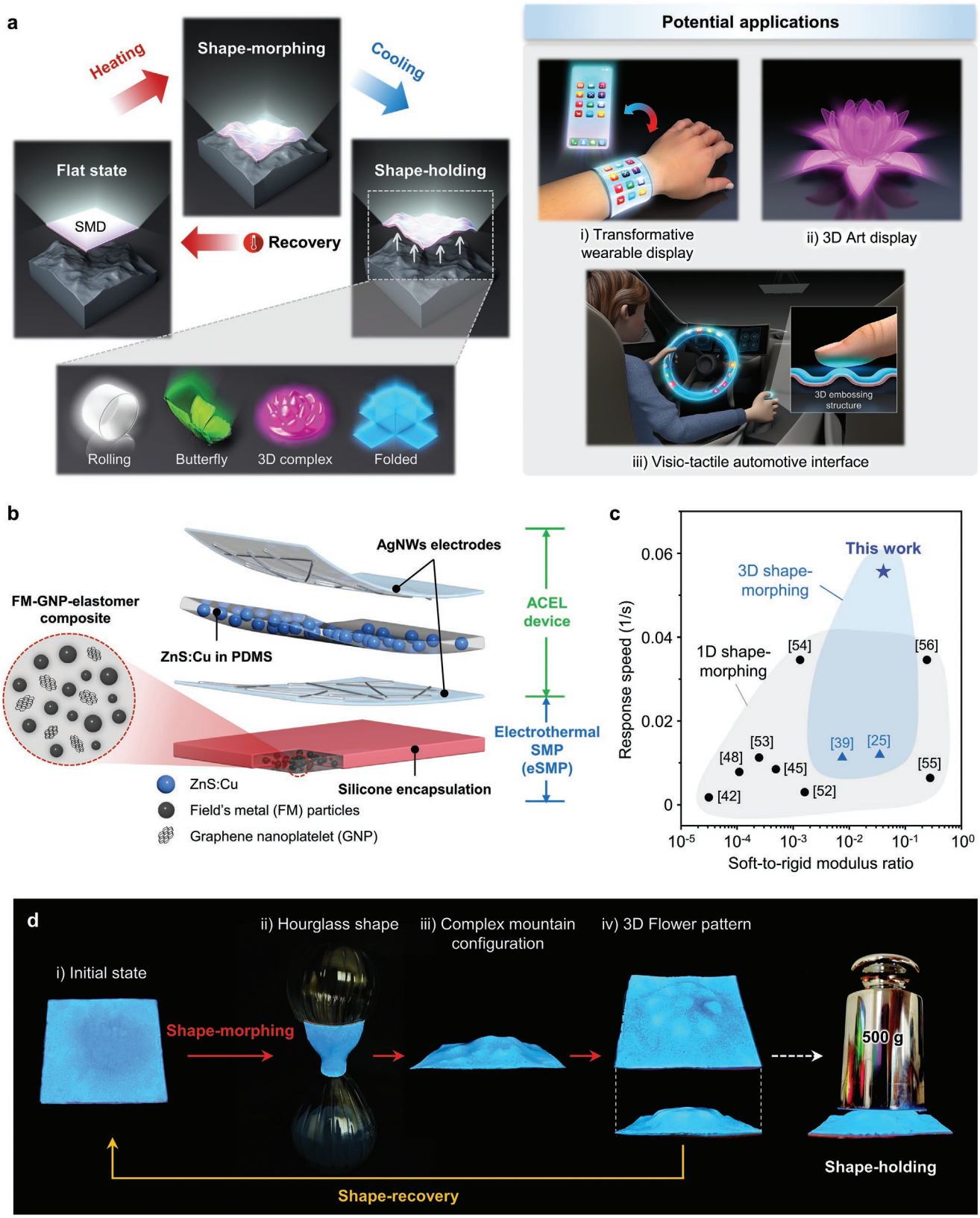


**Figure 1.** Concept and design of a shape-morphing display (SMD) featuring reversible shape reconfigurability and fixation. a) Schematic diagram illustrating the concept, the operational principle, and potential applications of the SMD, which can be morphed into robust 3D structures based on thermally-driven stiffness tuning. The SMD can be of use in various applications, including i) a transformative wearable display that converts between

 

and thermal conductivities of the eSMP, GNPs are added to the FM microparticles-embedded elastomeric composite. This additive produces a synergistic effect on thermally-driven shape programmability by enabling rapid and uniform phase transition (activation time < 30 s) across the platform during joule heating via electrothermal actuation. The stretchable ACEL device, which is the other major component, is constructed with a sandwiched structure where a ZnS:Cu/PDMS layer (Figure S1a, upper right, Supporting Information) is inserted in between a pair of transparent and stretchable silver nanowire (AgNW) electrodes (Figure S1a, bottom right, Supporting Information).[47] Owing to the phosphorescent property of ZnS:Cu phosphor, the device emits light based on the hot-electron impact excitation mechanism caused by the applied voltage.[46,50,51] As shown in Figure 1c, SMDs, which possess rapid response speed for electrothermal operation and adequate rigid-soft conversion, are capable of exceptional 3D shape reconfiguration.[25,39,42,45,48,52–56]

Figure 1d shows a proof-of-concept demonstration of the reprogrammable shape-morphability and shape-latchability of the SMD. Following the above working mechanism (Figure 1a), a planar SMD can be sequentially transformed into various multi-stable 3D structures. Upon electrothermal mode switching to the soft state, it can deform and stretch to conformally reconfigure along the surface of 3D objects, such as an hourglass, a complex mountain model, and a flower pattern. Returning to the rigid mode at room temperature, the morphologically reconfigured SMD exhibits load-bearing ability due to the structural robustness induced by the solid-state FM microparticles within the eSMP. The unique features of 3D shape morphing and holding can not only overcome the limitations of conventional manufacturing, which makes the creation of displays with unconventional 3D structures arduous, but also enable new applications of displays beyond those offered by the current ones with flat, flexible, foldable, or rollable forms.

## 2.2. Preparation of eSMP and its Electrothermal Characteristics

### *2.2.1. Fabrication of eSMP*

Our eSMP, which is a 3D shape-morphing system for the SMD, is prepared by dispersing molten FM in a PDMS solution blended with GNPs by manual stirring, as shown in Figure S2 (Supporting Information). The detailed fabrication process is described in the experimental section. The resulting FM-GNP-PDMS composite can be manufactured in various patterns by using different 3D-printed molds (Figure S3, Supporting Information). In general, interfacial voids are generated due to a dewetting between a polymer matrix and non-functionalized GNPs during the mixing process.[57,58] However, when rolling and pressing are applied with a pressure of 4.3 kPa or higher in the eSMP molding process, existing cavities are removed by mechanical compression on the surface. This forms a percolation network of FM microparticles and GNPs within the eSMP to create conductive pathways that substantially improve the electrical conductivity (from 18.2 to 3570.8 S $m^{-1}$), therefore thermal conductivity, across the platform (**Figure 2**a). Subsequently, the cured platform is encapsulated with silicone with high toughness (RT623, ELASTOSIL; 7.5 N $mm^{-2}$) to prevent possible leakage of liquified FM during extreme deformation in the soft mode. Figure 2b shows a photograph of the completed eSMP. The surface of our eSMP is highly flat and smooth (the average surface roughness = 86 nm. Figure S4 in the Supporting Information) so it can be used as a substrate to allow facile integration or direct fabrication of other electronic device layers for its functional versatility[59] (Figure S5, Supporting Information). Raman spectroscopy (irradiation at 514 nm) confirms the inclusion of GNPs in the eSMP as indicated by D, G, and 2D peaks at 1353, 1578, and 2721 $cm^{-1}$ (Figure 2c),[60] which facilitates uniform and rapid electrothermal shape reconfiguration of the platform.

### *2.2.2. Electrothermal Characterization of eSMP*

Understanding and analyzing the electrothermal behavior of an eSMP is important to optimizing the shape reconfiguration operation of the SMD due to its thermally-induced stiffness tunability. Figure 2d,e shows the temperature responses of the eSMP in the thawing and freezing processes, respectively. Note that $t_m$ in Figure 2d and $t_c$ in Figure 2e each respectively represent the time required for the eSMP to be fully softened during heating and fully solidified during freezing. In the thawing process, a phase transition occurs at nearly 62 °C, the melting temperature of FM (Figure 2d). On the other hand, in the freezing process, the liquid-state FM microparticles are crystallized at a temperature slightly below 62 °C due to supercooling[45] (Figure 2e). However, the supercooling is not of concern for our eSMP because of the intrinsic property of FM exhibiting a substantially smaller degree of supercooling (ΔT: a few degree), compared to other liquid metals (e.g., ΔT of gallium: up to a few tens of degree). Besides, the size of liquid metal particles is an important factor in determining the extent of supercooling, in which more prominent supercooling occurs as the FM particle size gets smaller.[52,61–63] In our eSMP, the particle size of FM is optimized to be between 30 μm and 50 μm (average ≈ 45.67 μm; Figure S6, Supporting Information) to enable rapid liquid-to-solid phase transition with the minimal supercooling phenomenon (ΔT ≈1.9 °C).

GNPs play a critical role in the electrothermal behavior of the eSMP, enabling rapid rigid-soft mode conversion through

the handheld and the wristband form, ii) a 3D art display such as the one mimicking flower blooming, and iii) a visio-tactile automotive interface that can offer 3D touch-sensing. The inset in the bottom image of potential applications (i.e., "visio-tactile automotive interface") shows the cross-sectional image of the embossing structure of SMD. b) Exploded-view schematic diagram of SMD, consisting of stretchable alternating current electroluminescent (ACEL) device and electrothermal shape-morphing platform (eSMP) built with FM-GNP-elastomer composite. c) Comparison of response speed and soft-to-rigid modulus ratio of liquid metal based stiffness-tunable materials. d) Sequential optical images demonstrating the programmable shape-morphability of SMD that can be transformed into a variety of complex 3D structures (e.g. hourglass, mountain, and flower shapes) to retain its shape and withstand heavy load. The rightmost image shows an example of SMD supporting a 500 g of weight.

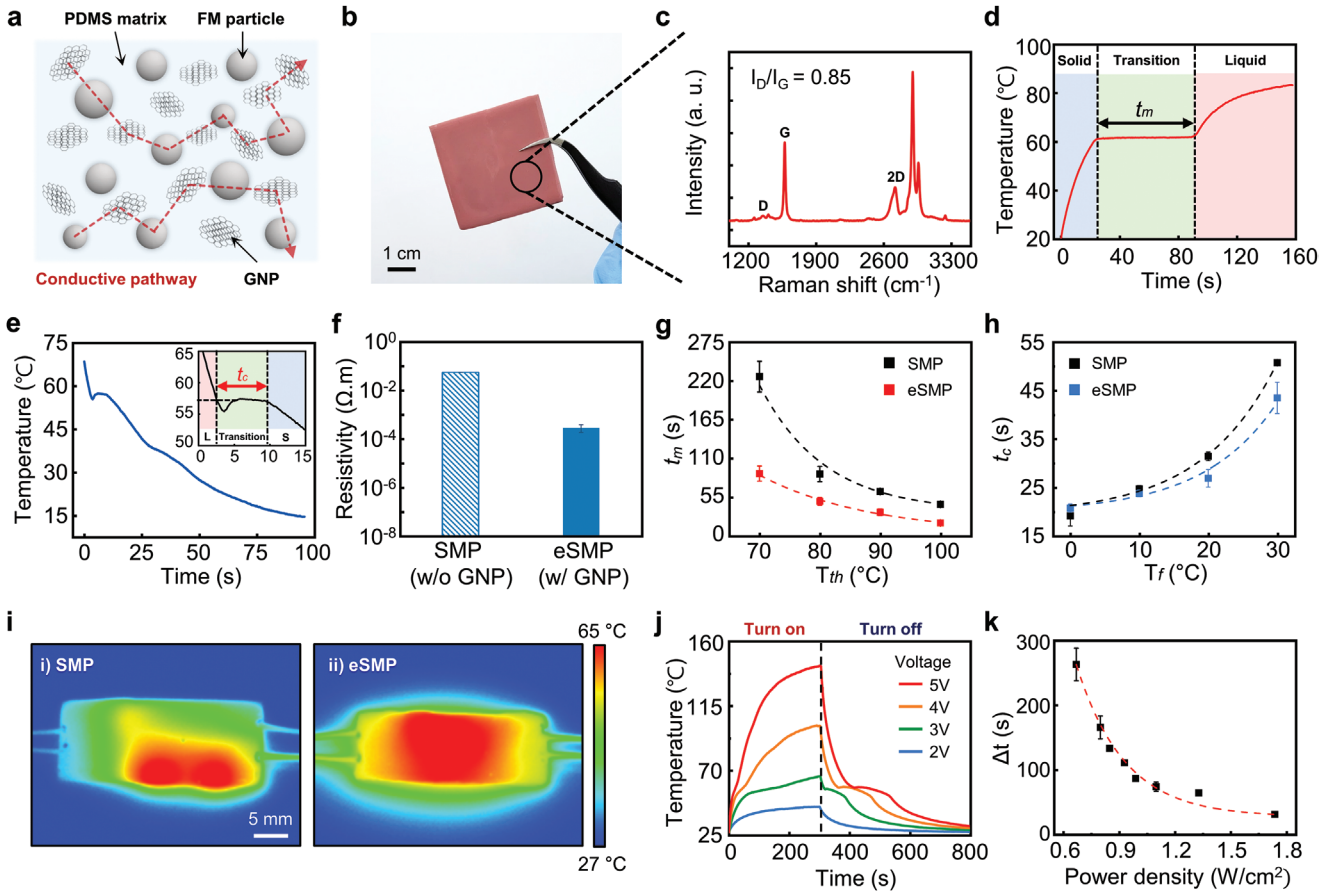


**Figure 2.** Electro-thermal studies of phase change behavior of electrothermal shape-morphing platform (eSMP). a) Schematic illustration that shows the inner structure of eSMP, where FM microparticles and GNP form electrically conductive pathways within the elastomer matrix. b) Optical image of eSMP. c) Raman spectrum of FM-GNP-PDMS composite exhibiting D (1353 $cm^{-1}$), G (1578 $cm^{-1}$), and 2D (2721 $cm^{-1}$) bands characteristic of GNP. d,e) Plot showing phase transition of the platform (i.e., rigid to soft mode or vice versa) during d) melting and e) freezing of FM particles. f) Electrical resistivity of SMP and eSMP, highlighting improved electrical conductivity of eSMP by admixing of GNP. g) Phase transition time ($t_m$) of SMP (without GNP addition) and eSMP (with GNP addition) as a function of applied thawing temperature ($T_{th}$) during the rigid-to-soft conversion ($n = 5$). h) Time required for phase transition ($t_c$) of SMP and eSMP under different freezing temperatures ($T_f$ = 0, 10, 20, and 30 °C) during the soft-to-rigid conversion. The error bars represent the standard deviation ($n = 5$). i) Infrared (IR) thermal images of (i) SMP and (ii) eSMP (sample size (mm): 30 ($l$) × 13 ($w$) × 1.5 ($t$)), joule heated with an applied voltage of 3 V. eSMP makes uniform heating across the platform facilitating the phase change (i.e., softening) of the entire device, while SMP suffers from localized heating. j) Temperature profile of eSMP during joule heating at various applied voltages (2, 3, 4, and 5 V). k) The characteristic time ($\Delta t$) required for phase transition responding to joule heating under different power densities. Note that the characteristic time ($\Delta t$) is calculated by an elapsed time when the temperature of the platform reaches from 27 to 63 °C. The error bars represent the standard deviation of 5 repetitive measurements for each power density ($n = 5$).

enhancement of thermal and electrical conductivities, as mentioned previously. FM itself has high electrical conductivity ($1.92 \times 10^6$ S $m^{-1}$). However, despite the high concentration of FM microparticles in the polymer matrix, the SMP (without GNPs) exhibits low electrical conductivity (18.2 S $m^{-1}$) because of the difficulty in attaining the percolation threshold with spherical FM microparticles for sufficiently high electrical conductivity.[64] The addition of GNPs into the FM-PDMS composite helps to form a rich electrical network. With GNP inclusion, we were able to lower the resistivity of the platform nearly 200 times through the creation of conductive pathways between spherical FM microparticles and GNPs (resistivity: 0.06 Ω × m in SMP (without GNPs) vs $2.8 \times 10^{-4}$ Ω × m in eSMP (with GNPs); Figure 2f). Figure 2g,h highlights the effect of GNP inclusion on improving the thermal response of the platform, comparing the rigid-soft phase transition time of the SMP and the eSMP in thawing and freezing conditions, respectively. The measurement of the phase transition time is examined by monitoring the temperature change of the platforms with an infrared (IR) camera (A655sc, FLIR) over time. In both the SMP and eSMP, overall, $t_m$ tends to decrease with a higher thawing temperature ($T_{th}$), while $t_c$ decreases along with a lower freezing temperature ($T_f$). However, an increase in thermal conductivity in the eSMP due to the inclusion of GNPs brings out a notable reduction in $t_m$ and $t_c$ at every given $T_{th}$ and $T_f$, respectively, thereby allowing faster phase conversion between soft and rigid states (Figure 2g,h). For example, $t_m$ of the eSMP decreases by 60% compared to that of the SMP for $T_{th}$ of 100 °C, thus exhibiting a significantly short phase transition time ($t_m$ = 18 s). In the freezing process, the eSMP shows a 17% decrease in phase change time ($t_c$ = 27 s) for $T_f$ of 20 °C. In addition, GNPs in the eSMP enable a uniform thermal response across the platform

during electrothermal operation. Figure 2i visualizes heat dissipation across the SMP and eSMP during Joule heating; the SMP shows a localized hot spot due to its nonuniform and poor electrical properties, while the eSMP exhibits a highly uniform temperature response. The spatially uniform heat distribution in electrothermal actuation is an essential attribute for the eSMP to provide reliable and rapid shape programming.

To determine the electrothermal operation condition of the eSMP, its thermal response is characterized during Joule-heating. Figure 2j exhibits the transient temperature profiles of the eSMP under different applied biases. When the applied voltage is higher than 3 V (i.e., $V_{bias}$ = 4 V or 5 V), the eSMP reaches the phase transition temperature (62 °C), allowing its conversion to the soft state for shape morphing without the need for an external heat source (e.g., hot plate, hot air gun, etc.). Since the nucleation temperature of FM is much higher than room temperature, the eSMP spontaneously and rapidly goes back to the rigid state as soon as the power is turned off. The time required for the eSMP to reach the phase transition temperature (≈62 °C) from room temperature via electrothermal actuation decreases with a higher applied power, dropping to ≈30 s at a power density of 1.74 W $cm^{-2}$ (Figure 2k). Overall, the eSMP achieves rapid conversion between bistable soft and rigid states through electrothermal actuation and thus supports reliable shape reconfiguration and fixation.

### 2.3. Thermomechanical Analysis of eSMP and its Shape Memory Behavior

In order to investigate the thermomechanical behavior of the eSMP, we examined the thermally-driven stiffness variation and its concomitant shape memory behavior of our eSMP. The eSMP exhibits two critical mechanical features: i) outstanding load-bearing property in the rigid state for shape fixation and ii) excellent stretchability and deformability in the soft state for shape reconfiguration. **Figure 3**a visualizes the effect of the amount of FM inclusion in the eSMP on load-bearing ability. Among the morphed eSMPs with different volume ratios ($\Phi$ = 30, 50, and 70%), the eSMP containing $\Phi$ = 70% FM could withstand the highest weight (50 g), exhibiting its remarkable mechanical robustness. In addition to the load-bearing ability, the stiffness tuning ratio (denoted as $E_{rigid}/E_{soft}$, where $E_{rigid}$ and $E_{soft}$ are the elastic moduli in the rigid and soft states, respectively) by solid-liquid phase transition of FM was compared under the same volume ratio conditions to find the optimal FM composition ratio for stiffness tuning. Based on the FM melting point of 62 °C, the platform can be in either the rigid state below 62 °C or the soft state above it. The elastic moduli of SMPs (FM-PDMS composite) differ according to the FM volume ratio, leading to distinct stiffness tuning ratios. Figure 3b clearly shows that the stiffness tuning ratio increases with an increasing amount of FM. The SMP with $\Phi$ = 70% FM has the largest stiffness tuning ratio of 7.22 with the highest elastic modulus of 14.29 MPa in the rigid state compared to that of the SMP with less FM (i.e., stiffness tuning ratio of 3.21 at $\Phi$ = 30% FM and 6 at $\Phi$ = 50% FM). Given the remarkable load-bearing capability and high stiffness variation, we considered the platform with $\Phi$ = 70% FM the most suitable for SMD use.

Adding 1 wt.% GNPs as a conductive additive to an FM-PDMS composite further increases the elastic modulus of the eSMP as well as the stiffness tuning ratio. Figure 3c compares the elastic moduli of the SMP (without GNPs; dotted line) and the eSMP (with GNPs; solid line) in both rigid and soft states to show the stiffening effect by the inclusion of GNPs other than enhancing the electrical and thermal conductivities. The elastic modulus of the eSMP (≈19.11 MPa) is ≈34% higher than that of the SMP (≈14.29 MPa) in the rigid state due to the stiffening effect through the incorporation of GNPs. On the other hand, in the soft state, the impact of adding GNPs was negligible. This is due to the voids formed by partially trapped hexadecane which is employed for the uniform dispersion of GNPs in the polymer matrix (Figure S7, Supporting Information), resulting in negligible variation in the overall mechanical properties. To sum up, we found that an eSMP consisting of 70% volume ratio of FM and 1 wt.% GNPs maximizes the practicality of the transformative platform by offering a large mechanical tuning (i.e., $E_{rigid}/E_{soft}$ ≈23.9).

Figure 3d highlights the shape morphing and fixation ability of our eSMP along with the change in FM particle morphology when stretched by 20% of its original length. While the initial state of the eSMP without any tensile strain exhibits spherical FM particle morphology, the FM microparticles of the stretched eSMP are elongated following the direction of applied strain due to the fluidity of liquefied FM microparticles in the soft state during transformation. The elongated FM microparticles can maintain their morphology through the cooling process, creating a supporting mechanical network structure within the eSMP to hold the deformed shape. When thermal stimulation is applied to the deformed eSMP, it returns to its original state due to the elastic nature of the composite. This mechanical property is referred to as "shape memory behavior". The shape memory behavior is evaluated by two important criteria: extent of shape fixity ($R_f$) and shape recovery ($R_r$). Shape fixity represents the ability to retain a deformed shape, while shape recovery quantifies the ability to return to its original state fully. To determine the shape memory characteristics of the eSMP for the degree of deformation, we measured the extent of shape fixity ($R_{f,1D}$) and shape recovery ($R_{r,1D}$) as a function of applied uniaxial tensile strain (Figure 3e). Note that $R_{f,1D}$ and $R_{r,1D}$ for uniaxial stretching are calculated as $R_{f,1D} = (\varepsilon_c/\varepsilon) \times 100\%$ and $R_{r,1D} = (1 - \varepsilon'/\varepsilon) \times 100\%$, where $\varepsilon_c$ and $\varepsilon$ are the current and the applied strain, respectively, and $\varepsilon'$ is the residual strain after the recovery process. In this experiment, we stretched a dog bone-shaped eSMP (36 mm ($l$) × 10 mm ($w$) × 1.2 mm ($t$)) up to the fracture point ($\varepsilon$ = 90%). As shown in Figure 3e, our eSMP shows a high extent of shape fixity and recovery according to applied tensile strains (e.g., $R_{f,1D}$ = 97.36% and $R_{r,1D}$ = 93.81% at $\varepsilon$ = 80%), verifying its excellent shape holding and restoration abilities after extreme deformation.

One distinct feature of our eSMP is an outstanding long-term shape memory performance in 3D morphed states for various applications. Figure 3f exhibits the exemplary sequential shape reconfiguration process of the eSMP, demonstrating a protruded complex 3D structure (e.g., alphabet "K"). For the characterization of 3D shape memory, the extent of shape fixity ($R_{f,3D}$) and shape recovery ($R_{r,3D}$) are measured for 14 days after the eSMPs are morphed into a dome shape with three

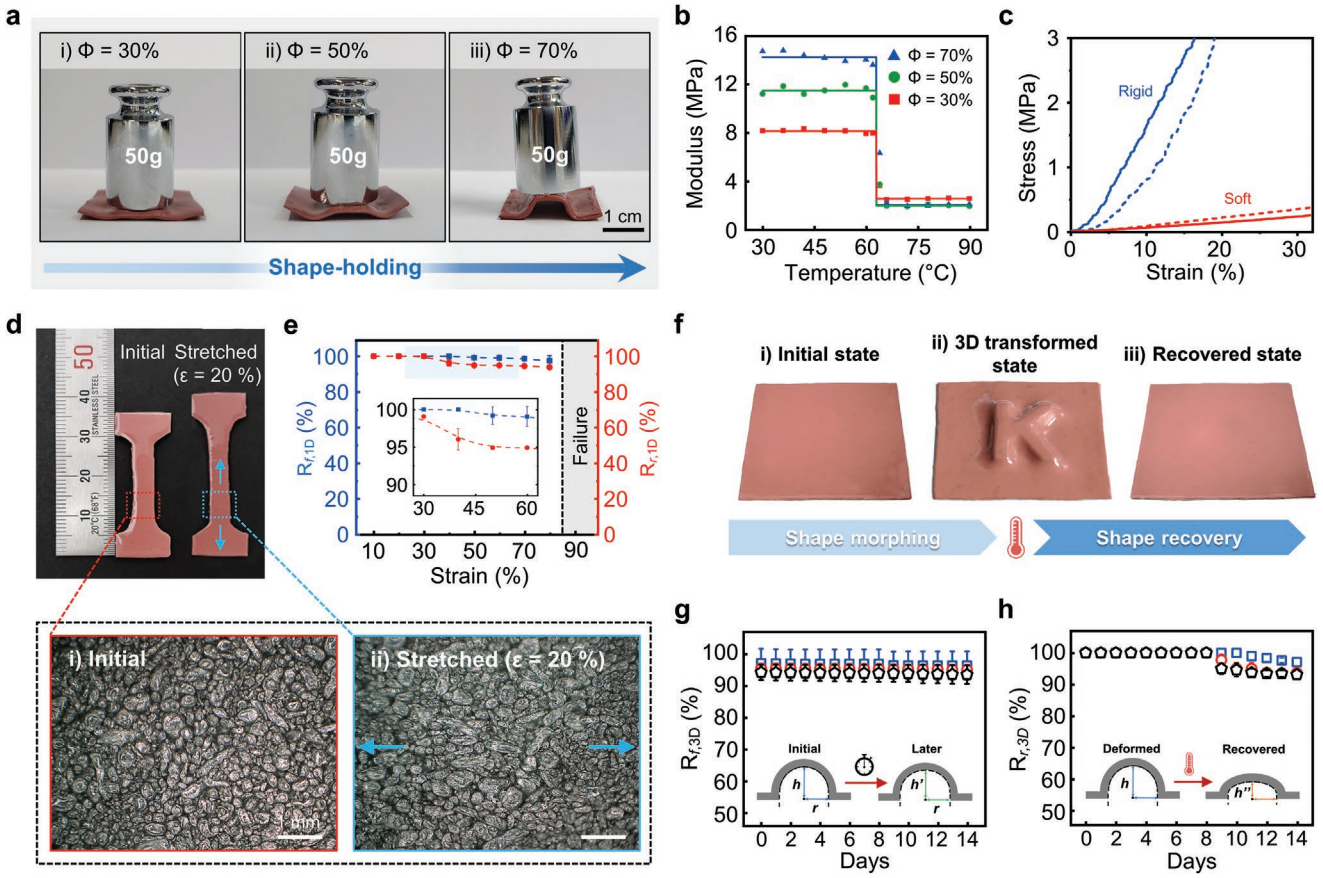


**Figure 3.** Mechanical and shape memory characteristics of eSMP. a) Photographs highlighting the load-bearing ability of eSMP with varying volume ratio (Φ) of FM, which determines shape-holding characteristics. b) Temperature dependence of elastic moduli of eSMP as a function of FM volume ratio. c) Stress-strain curves of eSMP (solid lines) and SMP (dashed lines) in the rigid and soft states. d) Photograph (top) highlighting the ability of eSMP to hold its shape after being stretched 20%. The bottom optical images show the cross-sectional morphologies of the FM-GNP-elastomer composite without (red box) and with tensile strain (blue box), corresponding to the initial and the stretched devices shown in the top image. e) Extent of shape fixity ($R_{f,1D}$) and recovery ($R_{r,1D}$) of the platform as functions of applied strain in the uniaxial direction. The error bars represent the standard deviation ($n = 3$). f) The sequential images showing the ability of eSMP that can return to the original shape from the 3D deformed state (i.e., shape memory capability). g) Extent of shape fixity of the deformed eSMPs as a function of time with different aspect ratio values ($h/r$) of dome-shaped deformation ($n = 3$ per group). Blue, red, and black dots represent data obtained from the deformed dome-shape eSMPs with the aspect ratio ($h/r$) of 0.33, 0.67, and 1, respectively. The extent of shape fixity ($R_{f,3D}$) is defined as $R_{f,3D} = (h'/h) \times 100\%$, where $h$, and $h'$ are the height of the initial deformed state and the current deformed state, respectively. h) Extent of shape recovery of the deformed eSMPs from the dome-shape with varying aspect ratio values ($h/r$) as a function of the deformed period after being shape morphed ($n = 3$ per group). The extent of shape recovery ($R_{r,3D}$) is defined as $R_{r,3D} = (\Delta h/h) \times 100\%$, where $\Delta h = h - h''$ is a change of the height of the deformed state after the recovery process and $h''$ is the remaining height after recovery transition.

different aspect ratios (ARs; $h/r = 0.33$, 0.67, and 1, where $h$ and $r$ represent the height and radius of the dome) (Figure 3g,h). In terms of the shape-holding ability for 3D deformation, a deformed shape with an AR of 0.33 shows the highest extent of shape fixity ($R_{f,3D}$ = 97.1%) compared to those with ARs of 0.67 ($R_{f,3D}$ = 95.5%) and 1 ($R_{f,3D}$ = 94.2%), indicating better shape-fixing ability with smaller deformation yet overall excellent shape maintainability regardless of the degree of deformation. Although the extent of shape fixity slightly decreases over time due to the elastic property of the polymer matrix, its value saturates at a certain point (i.e., Day 10) and still exhibits a high degree of shape fixity (i.e., $R_{f,3D}$ > 93% for A/R = 1) for all the cases, as shown in Figure 3g. This further verifies the excellent shape-fixing ability of our eSMP over time. It also shows good shape recovery ability, but the recovery rate degrades slightly faster over time compared to shape holdability because of the plastic deformation of the polymer matrix, inhibiting a complete recovery. With electrothermal actuation, the eSMP could completely recover its original shape (i.e., $R_{r,3D}$ = 100%) after being deformed for up to 8 days. After Day 8, the extent of shape recovery gradually decreased and eventually got saturated as the decline slowed down over time. The extent of shape restoration for all three cases (AR = 0.33, 0.67, and 1) on Day 14 still exceeded 93%, verifying its potential long-term utility as a shape memory platform.

### 2.4. SMD Characterization and its Potential Applications

Our proposed SMD can stably emit light under various shapes by integrating a highly deformable ACEL device with the eSMP. As shown in **Figure 4**a, a stretchable ACEL device is the

 

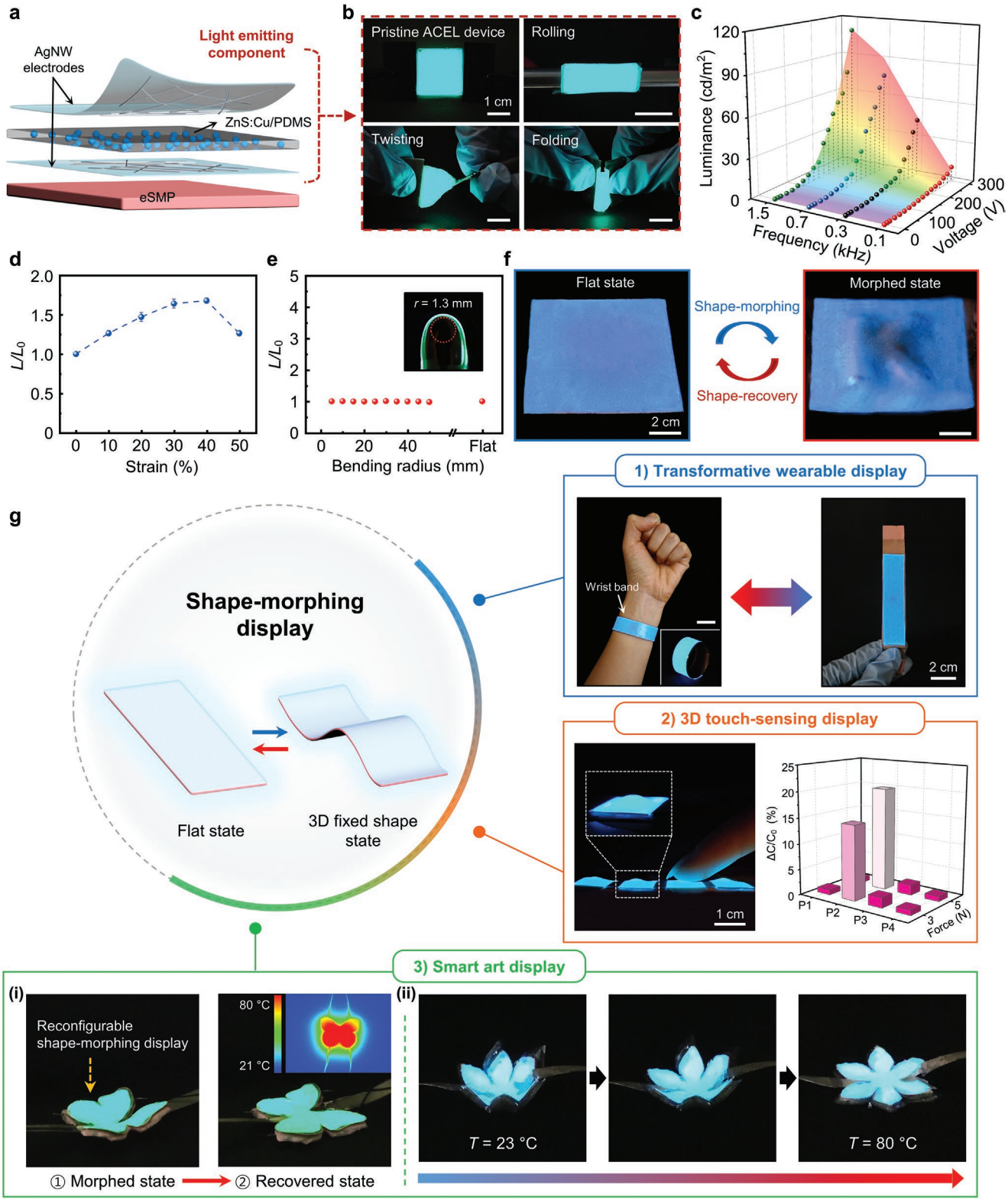


**Figure 4.** Diverse application demonstrations of electroluminescent SMD. a) Structural design of SMD integrating ACEL device as a light-emitting component, which consists of stretchable, transparent AgNW electrodes and ZnS: Cu/PDMS light-emitting layer. b) Optical images of the ACEL device under various deformations (i.e., rolling, twisting, and folding). c) Luminance of SMD as a function of applied voltage with different frequencies. The contour surface indicates theoretical data following the relationship between luminance and applied voltage. d,e) Relative luminance of SMD as functions of tensile strain (d) and bending radius (e) to confirm stable illumination under deformation. The error bars represent the standard deviation ($n = 3$). The inset shows a photograph of SMD bent with a bending radius of 1.3 mm (e). f) 3D topographical morphing and recovery of SMD. Optical

essential light-emitting component of the SMD to offer visual information. Owing to the long lifetime, chemical stability, and narrow emission spectrum[65] of its electroluminescent phosphor (ZnS:Cu; Figures S8 and S9, Supporting Information), the ACEL device can emit bright light induced by electric field-driven radiative recombination (Figure S10, Supporting Information). In addition, the AgNW electrodes covering the top and the bottom of the device exhibit sufficiently high transparency (light transmittance ≈76%; Figure S11a,b, Supporting Information), which allows efficient light emission. Based on its transparency and the high deformability (strain at break ≈180%; Figure S15a, Supporting Information) of the AgNW electrodes, the ACEL device shows stable luminance with uniform EL intensity under various mechanical deformations such as rolling, twisting, and folding (Figure 4b).

Figure 4c shows the change in luminance of our ACEL-integrated SMD according to the intensity and frequency of the applied AC voltage. The light intensity of the SMD increases with applied voltage and frequency after reaching a threshold voltage of 40 V (Figure S12, Supporting Information). The theoretical relationship between the luminance ($L$) of the SMD and the applied voltage ($V$) is expressed by $L = L_0 \exp(-\beta/V^{0.5})$, where $L_0$ and $\beta$ are empirical constants depending on device structure and materials.[66] The experimental results fit well with the theoretical value (Figure 4c). Meanwhile, the increase in frequency (from 100 to 700 Hz) shifts the EL intensity peak of the SMD from 495 to 459 nm at an applied voltage of 200 V (Figure S13a, Supporting Information). The frequency-dependent optical property can be confirmed by coordinates in the Commission Internationale de L'Eclairage (CIE) 1931 chromaticity diagram represented in Figure S13b (Supporting Information).

The SMD shows reliable luminescent properties under mechanical deformations such as stretching, bending, and 3D topographical morphing (Figure 4d–f; Figure S14, Supporting Information). Due to the high elasticity and stable mechano-electrical property of the AgNW electrodes (e.g., resistance change $(R/R_0) \approx 4.4$ at $\varepsilon = 40\%$; Figure S15b, Supporting Information), the optical characteristic of our SMD does not change significantly even with large stretching. For example, the luminous device can be elongated by 50% of its initial length without notable difference in brightness, as shown in Figure 4d and Figure S16 in the Supporting Information. The luminance of the SMD gradually increases until it is stretched up to a tensile strain of 40% due to the thickness reduction of the light-emitting layer, which reinforces the electric field within the electroluminescent layer. Above 40% strain, the luminance starts to decrease because of the increase in resistance of the AgNW electrodes (Figure S15b, Supporting Information). In terms of bending deformation, the SMD exhibits nearly constant luminance at any curvature, verifying its outstanding luminance reliability against bending deformation (Figure 4e). In addition, our SMD manifests an entirely consistent level of electroluminescence even under "3D topographical morphing", which is a unique characteristic that the conventional displays have not been able to achieve. Figure 4f represents that the SMD can maintain nearly constant light emission in the reversible process of transformation between the flat and the 3D morphed states with jagged deformation (e.g., alphabet "K" pop-up shape, protruding 5 mm). The long-term stability and durability of the SMD are verified by negligible luminance changes during 1000 cycles of bending and stretching (Figure S17, Supporting Information).

The shape reconfigurability with reliable luminescence of our SMD opens many new opportunities for a wide variety of applications, altering the way of using displays. Some exciting applications that will be enabled by SMD technology include 1) transformative wearable displays, 2) 3D touch-sensing displays, and 3) smart art displays (Figure 4g). An example of the transformative wearable display appears in the blue box of Figure 4g. The SMD could be utilized as an on-demand reconfigurable display that can convert between a wristband-type wearable display and a flat, handheld display depending on the user's necessity. A handheld, rigid display will provide ease of user interfacing (e.g., typing, web searching, etc.) due to its tractable even configuration and outstanding mechanical property much like the conventional flat panel electronics (e.g., mobile phones and laptops), while the wearable configuration will provide improved wearability and portability. Therefore, this transformative design can maximize user convenience as well as display utility through highly adaptive and versatile reconfiguration. Another potential application is the 3D touch-sensing display (Figure 4g, orange box). The SMD can turn into a capacitive touch-sensing display with unique 3D embossing structures to offer both visual information and facile, intuitive physical interaction by concurrently providing both visual and tactile senses. This application highlights the possibility of enabling multisensory cognition and feedback of users for various applications, including robotics, consumer electronics, and in-vehicle displays. Our SMD can also be of use in a smart art display that realizes 3D visual arts involving a dynamic physical motion for maximal aesthetic experience for users (Figure 4g, green box). Artistic, 3D-shaped designs of the SMD (e.g., butterfly or flower shapes) could be mechanically tuned using the shape memory effect, controlled by electrothermal actuation. Through the reliable shape reconfiguration by uniform thermal conduction, we were able to realize art displays with the flapping motion of butterfly wings (Figure 4g, green box, (i)) and the blooming of a

images show a reversible shape morphing involving localized stretching of SMD to form a complex 3D display (e.g., alphabet 'K'-structured display). g) Schematic diagram illustrating various applications of SMD for 1) transformative wearable display, 2) 3D touch-sensing display, and 3) smart art display. 1) Transformative wearable display that can convert between wristband (left) and handheld (right) configurations with high customizability. The inset in the left image shows a ring-shaped display that can be used in a form of a wristband or bracelet. 2) 3D touch-sensing display. Pixellated SMDs (1 × 4 arrays) with an embossing structure for enhanced tactility, along with capacitive touch sensing ability. The inset in the left image shows a magnified view of the SMD, highlighting the embossing shape. The right plot shows relative capacitance changes of SMD featuring a touch sensor with applied force, which presents capacitive sensing ability. 3) Smart art display. (i) Butterfly-shaped art display capable of actuating the flapping of wings through an electrothermal operation. The inset (right) shows the IR image of the device highlighting its ability to make a spatially-uniform temperature change during joule-heating. (ii) A flower-shaped art display that can mimic the blooming of a flower via electrothermal actuation.

flower (Figure 4g, green box, (ii); Video S1, Supporting Information). This smart art display can possibly achieve more complex, bi-directional motions by integrating reconfigurable actuators in its platform (e.g., shape memory alloy[67] and dielectric elastomer actuators[68]). All these proof-of-concept demonstrations verify the practical utility and versatility of the SMD along with its potential for diverse real-world applications, suggesting an innovative form factor for future displays.

### 2.5. Real-World Application of a 3D Touch-Sensing SMD for an Automotive System

Various types of touch-sensitive displays have been integrated with automobile components (e.g., middle console, rear-view mirror, and rear seat entertainment) as input systems to enable interaction between a driver and a vehicle. One promising strategy for the future human-vehicle interface is a visio-tactile system that provides both visual information and tactile cognition, improving the sensory feedback of drivers by allowing the driver to operate it without much interference from driving.[69] Therefore, this unusual display can work as a measure to enhance driving safety. Here, our 3D touch-sensing SMD, composed of a light-emitting device, a capacitive touch sensor, and an eSMP, allows visio-haptic sensing by providing 3D-structured tactile surfaces for enhanced sensory perception and interaction (**Figure 5**a). Figure 5b shows the 3D touch-sensing SMD designed for integration in an automotive system, where four SMD units (8 mm ($l$) × 12 mm ($w$), each; total dimensions: 43 mm ($l$) × 12 mm ($w$)) are serially

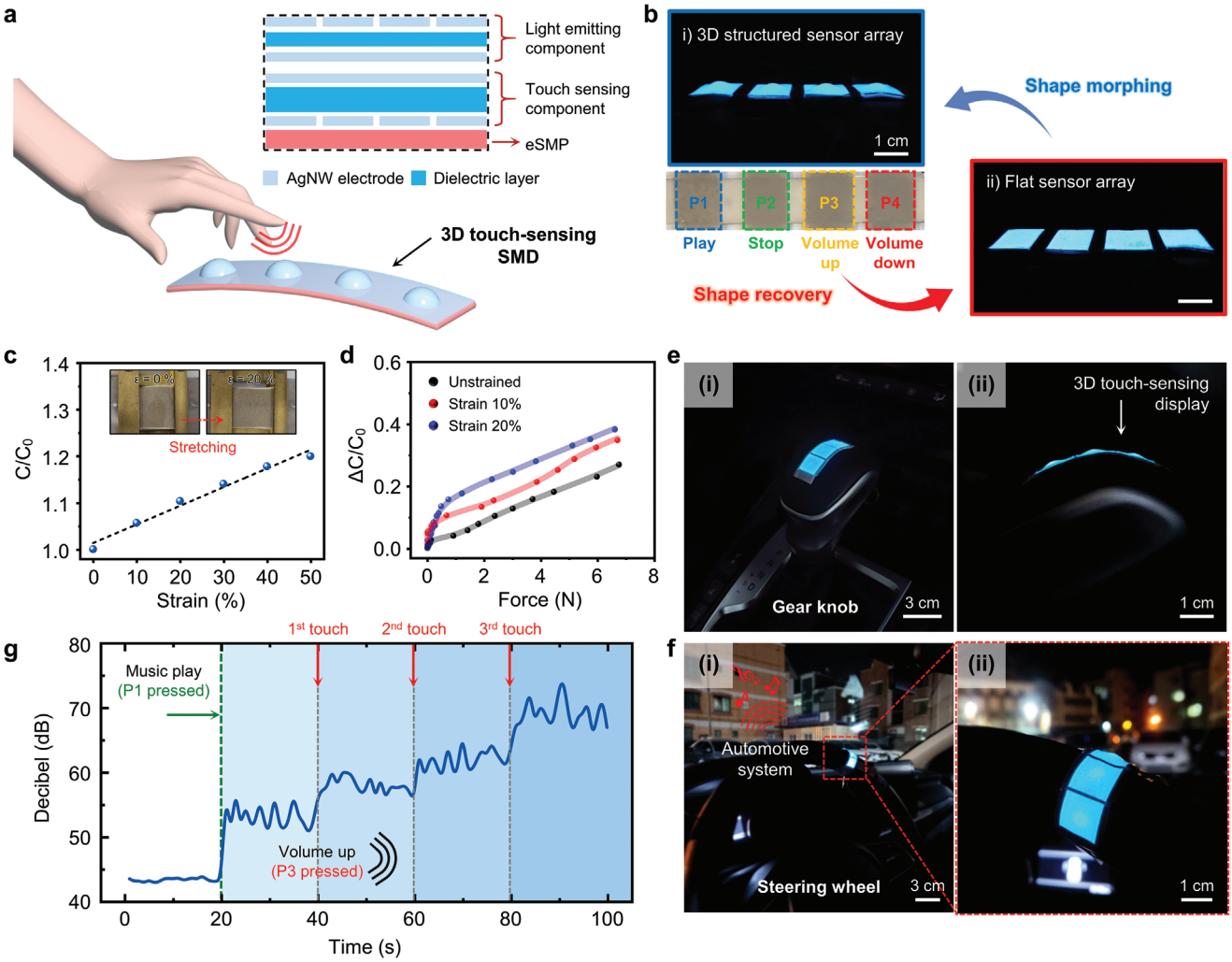


**Figure 5.** Application of a 3D touch-sensing SMD as an automotive display. a) Conceptual illustration of the 3D touch-sensing display. The inset shows a cross-sectional schematic architecture of the device. b) Optical images of two transformable states of 3D touch-sensing display with the 1 × 4 arrays: i) 3D structured state (working as embossing touch pads) for improved tactility, ii) Flat state. Each pixel performs a different function as an audio player in the vehicle (play, stop, volume up, and volume down). c) Normalized capacitance of the sensor as a function of applied tensile strain. The inset shows the sensor being stretched with 20% tensile strain. d) Relative capacitance changes of the sensor for unstrained and strained states ($\varepsilon$ = 0, 10, and 20%). e,f) Photographs of the 3D touch-sensing display integrated onto a e) gear knob; i) tilted view, ii) side view) and f) steering wheel; i) front view, ii) magnified view) for user-friendly, visio-tactile interfacing for control of the audio system. g) Plot illustrating the decibel level controls of the automotive audio system via the touch-sensing display.

integrated to control a music player during driving. Each pixel is built to provide a different function: music play (P1), stop (P2), volume up (P3), and volume down (P4). They are morphed into a convex protruding shape creating a tactile surface curvature on the display to elevate the touch perception and user-interactive features. Each planar pixel exhibits a consistent sensing response to the applied force, implying coherency of the sensing performance and outstanding device-to-device uniformity (Figure S19a, Supporting Information). In addition, the loading-unloading cyclic tests (1200 cycles with a maximum compressive force of 30 N) validate the high reliability and stability of our touch sensor (Figure S19b, Supporting Information). When stretched, the sensor shows a slight increase of static capacitance (Figure 5c). Nevertheless, Figure 5d shows that the capacitive sensor performs reliably for touch-sensing under applied pressure. This verifies the functional reliability of our touch-sensing SMD after 3D shape morphing.

Figure 5e,f shows the 3D touch-sensing SMD integrated with diverse automotive components (i.e., gear knob and steering wheel) to facilitate user-electronics interaction for music control based on its visio-tactile feature. The shape-morphing capability of the 3D touch-sensing SMD will enable its conformal integration on the curvilinear surface of a gear knob and a steering wheel, where the volume of a music player in the automotive system could be easily controlled with a simple finger touch (Figure 5g; Video S2, Supporting Information). This demonstration reveals the potential of touch-sensing SMDs for seamless integration with many other vehicle interior components as both smart user interfaces and aesthetic decorations. Further development of SMDs with electronically reversible 3D shape-reconfigurability coupled with a touch-sensing property may change the landscape of the user-interactive display, offering a smart interface convertible between a conventional flat display and a 3D multisensory communicative interface.

## 3. Conclusion

We have introduced a versatile SMD that can create complex 3D shapes and securely maintain the altered form. The most exciting aspect of the SMD is its ability to deliver immersive visual realism from user-interactive 3D structures. Additionally, the SMD can rapidly change into various forms through electrothermal operation, combining the features of both rigid and flexible/stretchable displays due to its ability to adjust stiffness. The SMD is achieved by integrating a stretchable ACEL device with an eSMP built using a FM-GNP-elastomer composite. This composite, a key for the eSMP, exhibits reliable and rapid electrothermal shape reconfiguration at a relatively low melting temperature (62 °C), enabling a unique shape-memory behavior with outstanding shape-fixing and recovery abilities. Owing to the stretchability and reliable illumination of the integrated ACEL device, our SMD exhibits stable electroluminescence under various 3D configuration modes such as folding, bending, and 3D topographical morphing. We have shown the potential of SMDs for various real-world applications through the successful demonstration of transformative wearable displays, dynamic 3D art displays, and visio-tactile in-vehicle user interfaces. With all these attractive features, our SMD could provide an opportunity to bring a new paradigm of display form factors that overcomes the limitation of existing display form factors. The SMD is compatible with existing inorganic and organic display manufacturing technologies, hence making its design and fabrication highly versatile.

For future research, various types of LMPA and other stimuli-responsive materials would need to be investigated to improve the mechanical deformability, durability, and reliability of the SMD. It is also important to note that our SMD currently operates within a low-strain range ($\varepsilon \approx 50\%$) due to the limited stretchability of AgNW electrodes.[70,71] Further studies need to be carried out to develop alternative electrodes[3,72–75] with giant stretchability and high transparency for ACEL devices to enable "freeform" 3D shape morphing. Additionally, the research could be conducted to develop a shape-morphing system that does not require manual structuring by incorporating active reconfigurable actuation mechanisms. We believe that continued research and development of SMD technology will lead to a broadening of its potential applications in the field of displays.

## 4. Experimental Section

*Fabrication of eSMP*: The eSMP was fabricated by casting a composite of FM (Roto144F, ROTOMETALS) microparticles, GNPs (US1059, US Research Nanomaterials Inc.), and PDMS elastomer. First, GNPs dispersed elastomer solution was prepared by mixing GNPs and PDMS (SYLGARD 184, Dow Corning) with hexadecane (99%, Sigma–Aldrich) in a weight ratio of 1:4:1 and stirred at 950 rpm for 12 h. Bulk FM with 70 vol.% was placed inside the resulting solution and warmed on a preheated hot plate (≈85 °C). Once the FM was completely molten, the two constituents were manually stirred until the molten FM was split into small particles and homogeneously dispersed. The mixture was poured into 3D-printed molds or cast into films. To form a flat surface with removed cavities, the sample was rolled and mechanically compressed using a roller. After rolling and pressing treatment, the sample was cured in the oven at 70 °C for 12 h. Finally, the fabricated platform was encapsulated with a tough silicone elastomer (RT 623 A/B, mixing ratio of 9:1, ELASTOSIL).

*Fabrication of Transparent AgNW Electrodes*: To fabricate AgNW electrodes, a glass substrate was prepared by cleaning with acetone, isopropyl alcohol (IPA), and deionized water. The sequentially cleaned glass substrate was treated with $O_2$ Plasma (100 W, 1 min) and placed on a heating plate at 80 °C. The AgNWs (average length = 50 µm, diameter = 70 nm; A70, Novarials) were dispersed in IPA with a weight ratio of 1:15 and detracted using a sonication bath. The well-dispersed AgNWs solution was uniformly spray-coated onto the glass substrate using an airbrush spray gun with an air pressure of 0.6 MPa. Then, the AgNWs-coated glass substrate was immersed in ethanol for 10 min to rinse out surfactants in the AgNWs network and placed at 100 °C to remove residual ethanol solvent. An as-prepared low-concentration SEBS (0.5 wt.% in toluene) solution was spin-coated (1000 rpm for 1 min) onto an AgNW-coated glass substrate to permeate the SEBS polymer into the AgNWs network. Next, the high-concentration SEBS (10 wt.% in toluene) solution was additionally spin-coated (1000 rpm for 1 min) and annealed at 100 °C for 30 min. The SEBS-coated substrate was treated with $O_2$ Plasma (100 W, 1 min). Finally, a prepolymer of PDMS with a 1:10 = curing agent:base weight ratio was spun onto the substrate at 500 rpm for 30 s and cured at 100 °C for 5 h. The resulting AgNW electrodes were easily peeled off from the glass substrate.

*Fabrication of SMD*: The SMD was fabricated through the integration of a stretchable ACEL device and an eSMP. To fabricate a stretchable ACEL device, a light-emissive layer was formed by admixing ZnS:Cu phosphor powder (LP-6844 and LP-6864, Fulcom (Marshal) Co.) and PDMS (PDMS base/curing agent, mixing ratio of 10:1) in a weight

ratio 2:1. The bottom AgNW electrode was prepared to clearly attach on a glass substrate showing the AgNW network upward. The ZnS:Cu/PDMS was degassed for 30 min and spin-cast on the bottom electrode at 2000 rpm for 60 s, followed by annealing at 70 °C for 30 min. The top AgNW electrode was gently laminated to the top of the light-emissive layer without a bubble trap and kept in a vacuum chamber at 70 °C for 6 h. Then, the fabricated ACEL device was delaminated from the glass carrier substrate and integrated on an eSMP using silicone (i.e, PDMS) as an adhesive.

*Mechanical Characterization*: The elastic modulus of the SMP was measured using a dynamic mechanical analyzer (DMA 850, TA Instruments) to examine the mechanical property under accurately controlled temperature variation. The specimens (20 mm ($l$) × 5 mm ($w$) × 1.2 mm ($t$)) including different FM volume content ($\Phi$ = 30, 50, and 70%) were mounted on the film tension clamp with the same torque force. The temperature ramp mode swept from 30 to 90 °C at a rate of 2 °C min$^{-1}$ was conducted with a loading frequency of 1 Hz. The compressive stress-strain curves for the platforms were obtained using a force gauge (M5-100, Mark-10). The compressive force and displacement data were recorded through MESUR Lite software to measure the information in real time. Both the SMP and eSMP specimens (11 mm ($l$) × 11 mm ($w$) × 4.5 mm ($t$)) were tested in rigid and soft states. For the temperature-dependent measurement, soft specimens were fully melted at the temperature above the FM melting temperature, while the rigid specimens were measured at room temperature.

*Characterization of Shape-Memory Behavior*: To evaluate the abilities of shape-fixity and recovery against applied strain, the dog-bone shaped eSMP specimens (36 mm ($l$) × 10 mm ($w$) × 1.2 mm ($t$)) were uniaxially stretched using a customized tensile testing instrument. The specimens were heated in the oven (70 °C) to be completely melted and stretched to a certain tensile strain (10% ≤ $\varepsilon$ ≤ 80%). The deformed specimens were kept at room temperature for 20 min to stabilize their states and removed from the instrument to measure the deformation. Then, the specimens were placed in the oven again to recover their original shape for 10 min and solidified to measure the residual deformation.

To cross-validate, the shape-memory behavior of eSMP was monitored by the 3D deformed platforms over time, which verified the reliability and durability of the platform from 3D deformation. The specimens (60 mm ($l$) × 60 mm ($w$) × 1.2 mm ($t$)) were heated at a temperature above 62 °C using a hot plate to soften the fabricated eSMP. The specimens in a soft state were placed on dome-shaped objects with different aspect ratios ($h/r$ = 0.33, 0.67, and 1, where h and r are the height and radius of the domes, respectively) produced by a 3D printer (Core 530, B9 Creations). Three-dimensionally deformed specimens were shaped using a vacuum chamber and fixed at room temperature. The extent of deformation was measured for 14 days using a digital height gauge and then the residual deformation was measured by applying heat to the deformed platform after a certain period of time (from day 1 to 14) to recover its shape.

*Characterization of SMD*: To supply the power into the SMD, a high-voltage amplifier (610C, TREK Inc.) coupled with a function generator (3390, KEITHLEY) was used to apply an alternating voltage to a stretchable ACEL device. The luminance, electroluminescent (EL) intensity spectra, and chromaticity coordinates of the SMD were measured with a spectroradiometer (CS-2000, Konica Minolta Inc.) in a dark room.

*Demonstration of 3D Touch-Sensing SMD for an Automotive System*: To implement the 3D touch-sensing SMD as a music player of an automotive system (K3, KIA motors), four capacitive sensing SMD arrays were connected to a capacitive touch sensor breakout board (MPR121, Adafruit) which communicated with an ATmega328 microcontroller (Arduino Nano, Adafruit). When pressing each sensor unit, the digitalized sensing output from the MPR121 was delivered to the microcontroller and processed using the custom-built Python software. Then, it was transmitted to the automotive audio system using Bluetooth communication. The audio output sound was measured by a digital sound level meter (DT-95, CEM), which was placed 10 cm away from the speaker. The decibel level controlled by the SMD touch sensor was recorded using the measurement software (Meterbox Pro, CEM software) in real time.

*Touch-Sensing Measurements under Deformed States in the 3D SMD*: For measurement of force/pressure output under various deformed states, the raw outputs of each pixel were calibrated and filtered in three levels using an Arduino-based breakout board (MPR121) in real time. In the first level of filtering, the number of touch-sensing pixels was obtained through an average data filter to identify the exact touch point. The second level of filtering provided the capacitance of the pressed pixel into 10-bit analog-to-digital conversion (ADC) counts. The third level of filtering produced the baseline value output, which represents the initial capacitance of the pixel (including original and deformed states) without force/pressure applied. These filtered data were used to determine the "touch" and "release" conditions by comparing the deviation between the capacitance under pressure (i.e., the second level filtered data output) and the baseline capacitance (i.e., the third level of filtered data output). The recognition sensitivity for the "touch" and "release" conditions were 12 counts and 6 counts, respectively. Consequently, the 3D touch-sensing SMD enabled reliable touch-sensing performance under various deformations. This was achieved by filtering and calibrating the initial capacitance (without force or pressure) value of each pixel in real time, followed by an automatic comparison process of filtered outputs to determine the relative capacitive change.

*Statistical Analysis*: The statistical data with error bars were shown as average value ± standard deviation (SD). The mean and SD for each set of samples were processed by Origin 2019 and Microsoft Excel software. The sample size (n) for mean and SD in thermal and joule heating characterizations (Figure 2g,h,k) was set $n$ = 5. The sample size (n) for mean and SD in shape-memory (Figure 3e,g,h), and light-emitting (Figure 4d,e) characterizations was set $n$ = 3. The touch-sensing properties of the 3D SMD were characterized by four measurements under the same applied pressure to ensure reproducibility.

## Supporting Information

Supporting Information is available from the Wiley Online Library or from the author.

## Acknowledgements

This work was supported by LG Display under LGD-KAIST Incubation Program (C2021004005) and the Basic Science Research Program through the National Research Foundation of Korea (NRF) funded by the Ministry of Science and ICT (NRF-2021R1A2C4001483).

## Conflict of Interest

The authors declare no conflict of interest.

## Data Availability Statement

The data that support the findings of this study are available from the corresponding author upon reasonable request.

## Keywords

3D display, electrothermal actuation, low melting point alloy, shape morphing display, stiffness tunability

Received: December 18, 2022
Revised: February 10, 2023
Published online:

[1] C. Wang, D. Hwang, Z. Yu, K. Takei, J. Park, T. Chen, B. Ma, A. Javey, *Nat. Mater.* **2013**, *12*, 899.
[2] G. H. Lee, H. Kang, J. W. Chung, Y. Lee, H. Yoo, S. Jeong, H. Cho, J.-Y. Kim, S.-G. Kang, J. Y. Jung, S. G. Hahm, J. Lee, I.-J. Jeong, M. Park, G. Park, I. H. Yun, J. Y. Kim, Y. Hong, Y. Yun, S.-H. Kim, B. K. Choi, *Sci. Adv.* **2022**, *8*, eabm3622.
[3] C. Larson, B. Peele, S. Li, S. Robinson, M. Totaro, L. Beccai, B. Mazzolai, R. Shepherd, *Science* **2016**, *351*, 1071.
[4] J. H. Koo, D. C. Kim, H. J. Shim, T.-H. Kim, D.-H. Kim, *Adv. Funct. Mater.* **2018**, *28*, 1801834.
[5] Y. H. Hwang, B. Noh, J. Lee, H. S. Lee, Y. Park, K. C. Choi, *Adv. Sci.* **2022**, *9*, 2104855.
[6] X. Shi, Y. Zuo, P. Zhai, J. Shen, Y. Yang, Z. Gao, M. Liao, J. Wu, J. Wang, X. Xu, Q. Tong, B. Zhang, B. Wang, X. Sun, L. Zhang, Q. Pei, D. Jin, P. Chen, H. Peng, *Nature* **2021**, *591*, 240.
[7] Z. Zhang, L. Cui, X. Shi, X. Tian, D. Wang, C. Gu, E. Chen, X. Cheng, Y. Xu, Y. Hu, J. Zhang, L. Zhou, H. H. Fong, P. Ma, G. Jiang, X. Sun, B. Zhang, H. Peng, *Adv. Mater.* **2018**, *30*, 1800323.
[8] B. Lee, J.-Y. Oh, H. Cho, C. W. Joo, H. Yoon, S. Jeong, E. Oh, J. Byun, H. Kim, S. Lee, J. Seo, C. W. Park, S. Choi, N.-M. Park, S.-Y. Kang, C.-S. Hwang, S.-D. Ahn, J.-I. Lee, Y. Hong, *Nat. Commun.* **2020**, *11*, 663.
[9] Z. Zhang, W. Wang, Y. Jiang, Y.-X. Wang, Y. Wu, J.-C. Lai, S. Niu, C. Xu, C.-C. Shih, C. Wang, H. Yan, L. Galuska, N. Prine, H.-C. Wu, D. Zhong, G. Chen, N. Matsuhisa, Y. Zheng, Z. Yu, Y. Wang, R. Dauskardt, X. Gu, J. B.-H. Tok, Z. Bao, *Nature* **2022**, *603*, 624.
[10] Y. Yang, T. Vervust, S. Dunphy, S. V. Put, B. Vandecasteele, K. Dhaenens, L. Degrendele, L. Mader, L. D. Vriese, T. Martens, M. Kaufmann, T. Sekitani, J. Vanfleteren, *Adv. Electron. Mater.* **2018**, *4*, 1800071.
[11] J. Choi, C. Han, S. Cho, K. Kim, J. Ahn, D. Del Orbe, I. Cho, Z.-J. Zhao, Y. S. Oh, H. Hong, S. S. Kim, I. Park, *Sci. Adv.* **2021**, *7*, eabj0694.
[12] X. Liu, D. Li, H. Fukutani, P. Trudeau, L. Khoun, O. Mozenson, K. L. Sampson, M. Gallerneault, C. Paquet, T. Lacelle, B. Deore, O. Ferrand, J. Ferrigno, P. R. L. Malenfant, A. J. Kell, *Adv. Electron. Mater.* **2021**, *7*, 2100194.
[13] T. Kim, J. S. Price, A. Grede, S. Lee, G. Choi, W. Guan, T. N. Jackson, N. C. Giebink, *Adv. Mater. Technol.* **2018**, *3*, 1800067.
[14] A. L. Bachmann, B. Hanrahan, M. D. Dickey, N. Lazarus, *ACS Appl. Mater. Interfaces* **2022**, *14*, 14774.
[15] C. Yang, H. Zhang, Y. Liu, Z. Yu, X. Wei, Y. Hu, *Adv. Sci.* **2018**, *5*, 1801070.
[16] D. C. Kim, H. Yun, J. Kim, H. Seung, W. S. Yu, J. H. Koo, J. Yang, J. H. Kim, T. Hyeon, D.-H. Kim, *Nat. Electron.* **2021**, *4*, 671.
[17] K. Zhang, Y. H. Jung, S. Mikael, J.-H. Seo, M. Kim, H. Mi, H. Zhou, Z. Xia, W. Zhou, S. Gong, Z. Ma, *Nat. Commun.* **2017**, *8*, 1782.
[18] Z. Song, T. Ma, R. Tang, Q. Cheng, X. Wang, D. Krishnaraju, R. Panat, C. K. Chan, H. Yu, H. Jiang, *Nat. Commun.* **2014**, *5*, 3140.
[19] S. Ji, B. G. Hyun, K. Kim, S. Y. Lee, S.-H. Kim, J.-Y. Kim, M. H. Song, J.-U. Park, *NPG Asia Mater* **2016**, *8*, 299.
[20] Y. Liu, B. Shaw, M. D. Dickey, J. Genzer, *Sci. Adv.* **2017**, *3*, 1602417.
[21] H. Luan, Q. Zhang, T.-L. Liu, X. Wang, S. Zhao, H. Wang, S. Yao, Y. Xue, J. W. Kwak, W. Bai, Y. Xu, M. Han, K. Li, Z. Li, X. Ni, J. Ye, D. Choi, Q. Yang, J.-H. Kim, S. Li, S. Chen, C. Wu, D. Lu, J.-K. Chang, Z. Xie, Y. Huang, J. A. Rogers, *Sci. Adv.* **2021**, *7*, eabj3686.
[22] S. Xu, Z. Yan, K.-I. Jang, W. Huang, H. Fu, J. Kim, Z. Wei, M. Flavin, J. McCracken, R. Wang, A. Badea, Y. Liu, D. Xiao, G. Zhou, J. Lee, H. U. Chung, H. Cheng, W. Ren, A. Banks, X. Li, U. Paik, R. G. Nuzzo, Y. Huang, Y. Zhang, J. A. Rogers, *Science* **2015**, *347*, 154.
[23] S. W. Song, S. Lee, J. K. Choe, N.-H. Kim, J. Kang, A. C. Lee, Y. Choi, A. Choi, Y. Jeong, W. Lee, J.-Y. Kim, S. Kwon, J. Kim, *Sci. Adv.* **2021**, *7*, eabf3804.
[24] Y. Kim, H. Yuk, R. Zhao, S. A. Chester, X. Zhao, *Nature* **2018**, *558*, 274.
[25] M. J. Ford, C. P. Ambulo, T. A. Kent, E. J. Markvicka, C. Pan, J. Malen, T. H. Ware, C. Majidi, *Proc. Natl. Acad. Sci.* **2019**, *116*, 21438.
[26] S. Li, H. Bai, Z. Liu, X. Zhang, C. Huang, L. W. Wiesner, M. Silberstein, R. F. Shepherd, *Sci. Adv.* **2021**, *7*, eabg3677.
[27] Y. Alapan, A. C. Karacakol, S. N. Guzelhan, I. Isik, M. Sitti, *Sci. Adv.* **2020**, *6*, eabc6414.
[28] Y. Wang, M. Li, J.-K. Chang, D. Aurelio, W. Li, B. J. Kim, J. H. Kim, M. Liscidini, J. A. Rogers, F. G. Omenetto, *Nat. Commun.* **2021**, *12*, 1651.
[29] R.-H. Kim, D.-H. Kim, J. Xiao, B. H. Kim, S.-I. Park, B. Panilaitis, R. Ghaffari, J. Yao, M. Li, Z. Liu, V. Malyarchuk, D. G. Kim, A.-P. Le, R. G. Nuzzo, D. L. Kaplan, F. G. Omenetto, Y. Huang, Z. Kang, J. A. Rogers, *Nat. Mater.* **2010**, *9*, 929.
[30] H. Jinno, T. Yokota, M. Koizumi, W. Yukita, M. Saito, I. Osaka, K. Fukuda, T. Someya, *Nat. Commun.* **2021**, *12*, 2234.
[31] G.-H. Lee, Y. R. Lee, H. Kim, D. A. Kwon, H. Kim, C. Yang, S. Q. Choi, S. Park, J.-W. Jeong, S. Park, *Nat. Commun.* **2022**, *13*, 2643.
[32] C. Y. Kim, M. J. Ku, R. Qazi, H. J. Nam, J. W. Park, K. S. Nam, S. Oh, I. Kang, J.-H. Jang, W. Y. Kim, J.-H. Kim, J.-W. Jeong, *Nat. Commun.* **2021**, *12*, 535.
[33] K.-I. Jang, K. Li, H. U. Chung, S. Xu, H. N. Jung, Y. Yang, J. W. Kwak, H. H. Jung, J. Song, C. Yang, A. Wang, Z. Liu, J. Y. Lee, B. H. Kim, J.-H. Kim, J. Lee, Y. Yu, B. J. Kim, H. Jang, K. J. Yu, J. Kim, J. W. Lee, J.-W. Jeong, Y. M. Song, Y. Huang, Y. Zhang, J. A. Rogers, *Nat. Commun.* **2017**, *8*, 15894.
[34] H. Kim, J. A. Lee, C. P. Ambulo, H. B. Lee, S. H. Kim, V. V. Naik, C. S. Haines, A. E. Aliev, R. Ovalle-Robles, R. H. Baughman, T. H. Ware, *Adv. Funct. Mater.* **2019**, *29*, 1905063.
[35] M. Mattmann, C. De Marco, F. Briatico, S. Tagliabue, A. Colusso, X.-Z. Chen, J. Lussi, C. Chautems, S. Pané, B. Nelson, *Adv. Sci.* **2022**, *9*, 2103277.
[36] C. Majidi, R. J. Wood, *Appl. Phys. Lett.* **2010**, *97*, 164104.
[37] D. S. Shah, E. J. Yang, M. C. Yuen, E. C. Huang, R. Kramer-Bottiglio, *Adv. Funct. Mater.* **2021**, *31*, 2006915.
[38] T. L. Buckner, M. C. Yuen, S. Y. Kim, R. Kramer-Bottiglio, *Adv. Funct. Mater.* **2019**, *29*, 1903368.
[39] D. Hwang, E. J. Barron, A. B. M. T. Haque, M. D. Bartlett, *Sci. Robot.* **2022**, *7*, eabg2171.
[40] I. M. Van Meerbeek, B. C. Mac Murray, J. W. Kim, S. S. Robinson, P. X. Zou, M. N. Silberstein, R. F. Shepherd, *Adv. Mater.* **2016**, *28*, 2801.
[41] S.-H. Byun, J. Y. Sim, K.-C. Agno, J.-W. Jeong, *Mater. Today Adv.* **2020**, *7*, 100089.
[42] S.-H. Byun, J. Y. Sim, Z. Zhou, J. Lee, R. Qazi, M. C. Walicki, K. E. Parker, M. P. Haney, S. H. Choi, A. Shon, G. B. Gereau, J. Bilbily, S. Li, Y. Liu, W.-H. Yeo, J. G. McCall, J. Xiao, J.-W. Jeong, *Sci. Adv.* **2019**, *5*, eaay0418.
[43] M. D. Dickey, *Adv. Mater.* **2017**, *29*, 1606425.
[44] Y. Lin, J. Genzer, M. D. Dickey, *Adv. Sci.* **2020**, *7*, 2000192.
[45] S.-H. Byun, C. S. Kim, K.-C. Agno, S. Lee, Z. Li, B. J. Cho, J.-W. Jeong, *Adv. Mater.* **2021**, *33*, 2007239.
[46] J. Wang, C. Yan, K. J. Chee, P. S. Lee, *Adv. Mater.* **2015**, *27*, 2876.
[47] F. Stauffer, K. Tybrandt, *Adv. Mater.* **2016**, *28*, 7200.
[48] W. Shan, T. Lu, C. Majidi, *Smart Mater. Struct.* **2013**, *22*, 085005.
[49] O. Rohr, *Ind. Lubr. Tribol.* **2002**, *54*, 153.
[50] M. Dür, S. M. Goodnick, S. S. Pennathur, J. F. Wager, M. Reigrotzki, R. Redmer, *J. Appl. Phys.* **1998**, *83*, 3176.
[51] S. Li, B. N. Peele, C. M. Larson, H. Zhao, R. F. Shepherd, *Adv. Mater.* **2016**, *28*, 9770.
[52] S. Lee, S.-H. Byun, C. Y. Kim, S. Cho, S. Park, J. Y. Sim, J.-W. Jeong, *Adv. Mater.* **2022**, *34*, 2204805.
[53] Y. Hao, T. Wang, Z. Xie, W. Sun, Z. Liu, X. Fang, M. Yang, L. Wen, *J. Micromech. Microeng.* **2018**, *28*, 024004.

[54] A. Tonazzini, S. Mintchev, B. Schubert, B. Mazzolai, J. Shintake, D. Floreano, *Adv. Mater.* **2016**, *28*, 10142.
[55] H. Yufei, W. Tianmiao, F. Xi, Y. Kang, M. Ling, G. Juan, W. Li, presented at IEEE 36th Chinese Control Conf. , XX, Dalian, China **2017**.
[56] P. Bhuyan, Y. Wei, D. Sin, J. Yu, C. Nah, K.-U. Jeong, M. D. Dickey, S. Park, *ACS Appl. Mater. Interfaces* **2021**, *13*, 28916.
[57] K. J. Berean, J. Z. Ou, M. Nour, M. R. Field, M. M. Y. A. Alsaif, Y. Wang, R. Ramanathan, V. Bansal, S. Kentish, C. M. Doherty, A. J. Hill, C. McSweeney, R. B. Kaner, K. Kalantar-zadeh, *J. Phys. Chem. C* **2015**, *119*, 13700.
[58] M. G. Saborio, S. Cai, J. Tang, M. B. Ghasemian, M. Mayyas, J. Han, M. J. Christoe, S. Peng, P. Koshy, D. Esrafilzadeh, R. Jalili, C. H. Wang, K. Kalantar-Zadeh, *Small* **2020**, *16*, 1903753.
[59] N. Namdari, B. Mohammadian, P. Jafari, R. Mohammadi, H. Sojoudi, H. Ghasemi, R. Rizvi, *Mater. Horiz.* **2020**, *7*, 366.
[60] L. Bokobza, J.-L. Bruneel, M. Couzi, *Vib. Spectrosc.* **2014**, *74*, 57.
[61] P. R. Couchman, W. A. Jesser, *Nature* **1977**, *269*, 481.
[62] J. Ma, P. Zhang, *Mater. Adv.* **2021**, *2*, 7437.
[63] S. Çınar, I. D. Tevis, J. Chen, M. Thuo, *Sci. Rep.* **2016**, *6*, 21864.
[64] A. Mohammadi Nasab, T. L. Buckner, B. Yang, R. Kramer-Bottiglio, *Adv. Mater. Technol.* **2022**, *7*, 2100920.
[65] J. Huang, Y. Yang, S. Xue, B. Yang, S. Liu, J. Shen, *Appl. Phys. Lett.* **1997**, *70*, 2335.
[66] L. Wang, L. Xiao, H. Gu, H. Sun, *Adv. Opt. Mater.* **2019**, *7*, 1801154.
[67] X. Huang, K. Kumar, M. K. Jawed, A. Mohammadi Nasab, Z. Ye, W. Shan, C. Majidi, *Adv. Mater. Technol.* **2019**, *4*, 1800540.
[68] E. Hajiesmaili, D. R. Clarke, *Nat. Commun.* **2019**, *10*, 183.
[69] S. J. Breitschaft, S. Clarke, C.-C. Carbon, *Front. Psychol.* **2019**, *10*, 01470.
[70] B. S. Kim, J. B. Pyo, J. G. Son, G. Zi, S.-S. Lee, J. H. Park, J. Lee, *ACS Appl. Mater. Interfaces* **2017**, *9*, 10865.
[71] Y. Zhou, S. Cao, J. Wang, H. Zhu, J. Wang, S. Yang, X. Wang, D. Kong, *ACS Appl. Mater. Interfaces* **2018**, *10*, 44760.
[72] J. Zhang, Q. Lu, Y. Li, T. Li, M.-H. Lu, Y.-F. Chen, D. Kong, *ACS Mater. Lett.* **2021**, *3*, 1104.
[73] J. Wang, C. Yan, G. Cai, M. Cui, A. Lee-Sie Eh, P. S. Lee, *Adv. Mater.* **2016**, *28*, 4490.
[74] Q. Lu, Y. Zhou, X. Yin, S. Cao, X. Wang, D. Kong, *Research* **2021**, *2021*.
[75] C. H. Yang, B. Chen, J. Zhou, Y. M. Chen, Z. Suo, *Adv. Mater.* **2016**, *28*, 4480.